Kinematic α effect in the presence of a large-scale motion

Alice Courvoisier[*]

Department of Applied Mathematics, University of Leeds, Leeds LS2 9JT, United Kingdom

Eun-jin Kim

Department of Applied Mathematics, University of Sheffield, Sheffield S3 7RH, United Kingdom

We investigate how the addition of a large-scale steady motion, either shear or uniform flow, modifies the magnetic transport properties of a family of chaotic velocity fields with different correlation times. We compute numerically the kinematic α effect that those flows give rise to and show that it is reduced by the presence of a large-scale motion parallel to the large-scale magnetic field, except under certain conditions when it can be slightly enhanced via resonances. The α effect is shown to depend on the nature of the large-scale motion and on the temporal characteristics of the chaotic flow. These results highlight the strong influence that a shear or a uniform flow can have on the turbulent transport of magnetic fields.

I. INTRODUCTION

A. Background

Astronomical observations have revealed that most cosmic bodies are magnetically active and possess a global coherent magnetic field. In the Sun, for example, this large-scale component is responsible for the 11-year sunspot cycle. Such fields are believed to be the result of a "large-scale dynamo," whereby inductive motions within a conductive fluid are able to generate and sustain a magnetic field on scales larger than their own. This process is traditionally modeled within the framework of mean-field electrodynamics (MFE), a turbulence closure theory where small-scale effects are parametrized by transport coefficients [1,2]. These include the α effect, which is responsible for the regeneration of poloidal (toroidal) magnetic field from toroidal (poloidal) field, and an enhanced turbulent diffusivity or β effect.

Furthermore, astrophysical plasmas are often characterized by the presence of large-scale shearing motions. These can, for example, take the form of differential rotation, as in the solar tachocline, a thin layer of strong radial shear located at the base of the solar convection zone [3]. Combined with mean-field effects, shear is an essential ingredient for large-scale dynamo action. It can lead for instance to an $\alpha\omega$-dynamo—the classical model for the solar cycle [1], to an "incoherent α-shear dynamo" (see Sec. V C 3), or to a shear-current dynamo (see, e.g., [4–6]).

Until recently however the large-scale fluid motions were often solely included in the mean-field equations, without their effects on the evolution of the small scales taken into account. This cannot however be justified in general since a large-scale shear or a mean flow can dramatically alter the properties of the small-scale motions and therefore affect turbulent transport, as reviewed below.

B. Effects of shear

A stable shear flow can quench the intensity and transport properties of the turbulence by distorting and disrupting turbulent eddies, thus accelerating the forward cascade of energy and enhancing dissipation. Moreover, the presence of a strong shear impedes transport across its direction; in particular, transport barriers caused by shear flows are considered to be indispensable for the improvement of plasma confinement in fusion devices (see, e.g., [7–12]).

Similar effects are expected to occur in astrophysical plasmas. For example, the problem of transport quenching by shear in the tachocline has recently been investigated analytically by Kim and her collaborators. They included complex physical interactions between turbulence, magnetic fields, rotation (Rossby waves/inertial waves) and differential rotation, whose effects on small-scales are usually ignored in traditional solar and stellar modeling [13–17].

Furthermore, in the context of three-dimensional (3D) forced helical magnetohydrodynamic (MHD) turbulence, an analytical study by [18] showed that both α and β effects are severely quenched by a strong shear while being slightly enhanced for weak shear. This α-suppression by a shear flow was subsequently observed in numerical simulations by [19] and a slight increase in β for weak shear was reported by [6]. Similar results have been obtained for two-dimensional (2D) MHD turbulence where the severe quenching of magnetic diffusion by shear predicted by [20,21] has been confirmed in numerical simulations by [22], who highlighted the dual role of shear flows, which quench transport by shearing while enhancing it by resonance.

C. Effects of a uniform flow

Shear distortion is however not the only mechanism by which a large-scale motion can affect small-scale turbulence. Indeed, recent laboratory experiments by [23] show that the level of turbulence in a 2D flow can also be reduced via sweeping of the force-generated vortices by the mean flow.

While uniform flows may commonly be regarded to have no effect due to Galilean invariance, we emphasize that this

---

*alice@maths.leeds.ac.uk

is not always the case in turbulence where this invariance is broken by nontrivial external forcing, boundaries, etc [24]. It is instructive to examine this in more details. For stationary turbulence with wavenumber $\boldsymbol{k}$, the transformation to a frame comoving with a uniform flow $\boldsymbol{U}_0$ gives a nonzero frequency to the turbulence, $\omega_D = \boldsymbol{U}_0 \cdot \boldsymbol{k}$, by Doppler shift. The uniform flow therefore alters the properties of the turbulence, changing it to wavelike turbulence with frequency ω_D, thus leading to a reduction in transport (like Alfvén waves quenching magnetic diffusion [15,20]). For turbulence with a nonzero characteristic frequency ω_0, a uniform flow can induce resonance when $\omega_0 - \boldsymbol{U}_0 \cdot \boldsymbol{k} = 0$. This enhances transport since the overlap of resonant layers is an important source of irreversibility (in addition to molecular diffusion and stochasticity), which is necessary for turbulent transport.

D. Aims and structure of the paper

The previous section emphasizes the important effects that large-scale motions can have on turbulent transport. The purpose of this paper is to investigate these issues further by performing a systematic numerical study of the influence of a large-scale motion on the α effect driven by a family of chaotic flows with different statistical properties. We limit our investigations to the kinematic regime and consider velocity fields of the form

$$\boldsymbol{U}(x,y,t) = \boldsymbol{u}_k(x,y,t) + \boldsymbol{U}_{LS}, \tag{1}$$

where $\boldsymbol{u}_k$ is the small-scale flow and $\boldsymbol{U}_{LS}$ is a steady velocity field, chosen to be either uniform or sinusoidal to model a large-scale shear. Since the flows are prescribed, the large-scale motion does not affect the small-scale velocity field directly. We are therefore able to investigate how the kinematic α effect driven by a small-scale velocity field is altered by the addition of a large-scale flow through modification of the small-scale magnetic field only.

We take $\boldsymbol{u}_k$ from a family of space-periodic motions possessing a single spatial scale. Such flows have been utilized in the studies of transport coefficients since the pioneering work of [25]. The scalar transport properties of such flows and how they are affected by a mean motion, or sweep, is reviewed in [26]. The α effect was determined for steady, integrable cases by, e.g., [27,28] and the influence of a uniform flow was considered in an asymptotic study by [29]. Another related study by [30] looks at how the dynamo growth rate is enhanced when a uniform flow is present. The extension to time-dependent, chaotic flows with no mean has been considered by [31,32]. In the present paper, we extend this last model to include the effects of the large-scale motion $\boldsymbol{U}_{LS}$. We show that the α effect is reduced as the magnitude of $\boldsymbol{U}_{LS}$ is increased, except for certain values when resonance conditions are met. We also demonstrate that the precise variations in α depend on the large-scale motion used (shear or uniform flow) and on the time correlations in $\boldsymbol{u}_k$.

The remainder of this paper is organized as follows. In Sec. II we review the basics of mean-field electrodynamics and present an analytical calculation of the α effect for an idealized turbulent flow, in the presence of a uniform flow and under the first order smoothing approximation. Although it is performed under very restrictive assumptions, this calculation illustrates some essential features of the resonances mentioned above. In Sec. III we setup both the shear and the uniform flow models and explain the method we use to determine the α effect. Since the chaotic properties of a flow influence its transport properties (see, e.g., [33]), we describe in Sec. IV how the Lagrangian chaos present in $\boldsymbol{u}_k$ is modified by the addition of a large-scale motion. Finally, we present the results of our numerical MHD simulations in Sec. V and conclude in Sec. VI.

II. MEAN-FIELD ELECTRODYNAMICS IN THE PRESENCE OF A LARGE-SCALE FLOW

A. General framework

The evolution of a kinematic magnetic field $\boldsymbol{B}$ embedded in a conducting fluid with velocity $\boldsymbol{U}$ is given by the dimensionless magnetic induction equation

$$\partial_t \boldsymbol{B} = \nabla \times (\boldsymbol{U} \times \boldsymbol{B}) + \mathrm{Rm}^{-1} \nabla^2 \boldsymbol{B}, \tag{2}$$

where Rm is the magnetic Reynolds number. In the mean-field paradigm, $\boldsymbol{B}$ is decomposed into the sum of its mean and fluctuating parts $\langle \boldsymbol{B} \rangle + \boldsymbol{b}$, where $\langle \cdot \rangle$ denotes a suitable averaging operation; similarly, $\boldsymbol{U} = \langle \boldsymbol{U} \rangle + \boldsymbol{u}$. The evolution equations for the mean and fluctuating magnetic fields are then given by

$$\partial_t \langle \boldsymbol{B} \rangle = \nabla \times \boldsymbol{\mathcal{E}} + \nabla \times (\langle \boldsymbol{U} \rangle \times \langle \boldsymbol{B} \rangle) + \mathrm{Rm}^{-1} \nabla^2 \langle \boldsymbol{B} \rangle, \tag{3}$$

and

$$(\partial_t - \mathrm{Rm}^{-1} \nabla^2) \boldsymbol{b} - \nabla \times (\boldsymbol{u} \times \boldsymbol{b} - \boldsymbol{\mathcal{E}})$$
$$= \nabla \times (\boldsymbol{u} \times \langle \boldsymbol{B} \rangle + \langle \boldsymbol{U} \rangle \times \boldsymbol{b}), \tag{4}$$

respectively, where $\boldsymbol{\mathcal{E}} = \langle \boldsymbol{u} \times \boldsymbol{b} \rangle$ is the mean electromotive force (emf). Since Eq. (4) is linear in $\langle \boldsymbol{B} \rangle$, $\boldsymbol{\mathcal{E}}$ can be expanded in terms of the mean field $\langle \boldsymbol{B} \rangle$ and its gradient as

$$\boldsymbol{\mathcal{E}} = \boldsymbol{\alpha} \cdot \langle \boldsymbol{B} \rangle + \boldsymbol{\beta} \cdot \nabla \langle \boldsymbol{B} \rangle + \cdots. \tag{5}$$

This expression defines the transport pseudotensors $\boldsymbol{\alpha}$ and $\boldsymbol{\beta}$, which depend on the properties of the flow $\boldsymbol{U}$ and on Rm [1,2]. Substitution of Eq. (5) into Eq. (3) leads to a closed evolution equation for the mean magnetic field, which can be solved in isolation provided the transport tensors are known. Here we focus on the α effect, which corresponds to the symmetric part of $\boldsymbol{\alpha}$ and is nonzero only if $\boldsymbol{U}$ lacks reflectional symmetry, e.g., if it is helical. It can be determined by solving Eq. (4) for a constant mean field $\boldsymbol{B}_0$. If we also consider a constant mean flow $\boldsymbol{U}_0$, Eq. (4) becomes

$$(\partial_t - \mathrm{Rm}^{-1} \nabla^2) \boldsymbol{b} - \nabla \times (\boldsymbol{u} \times \boldsymbol{b}) = (\boldsymbol{B}_0 \cdot \nabla) \boldsymbol{u} + (\boldsymbol{U}_0 \cdot \nabla) \boldsymbol{b}, \tag{6}$$

while Eq. (5) reduces to $\boldsymbol{\mathcal{E}} = \boldsymbol{\alpha} \cdot \boldsymbol{B}_0$.

B. Resonance effect

In this section, we use the classical calculation of the α effect driven by a small-scale, homogeneous, stationary, and isotropic turbulent velocity field $\boldsymbol{u}(\boldsymbol{x}, t)$ detailed in [1] to illustrate how resonances arise when a uniform flow $\boldsymbol{U}_0$ is

present. We use the first-order smoothing approximation (FOSA), which is valid for Rm ≪ 1 or Sr ≪ 1, where the Strouhal number Sr is the ratio of the correlation time to the turnover time of the turbulence. FOSA is unlikely to be strictly applicable to astrophysical situations, where Rm ≫ 1 and Sr ∼ 1; nevertheless the calculation below provides a useful insight into the behavior of the α effect in the presence of a uniform flow. Here we consider dimensional quantities, so formally, we use the magnetic diffusivity η instead of the magnetic Reynolds number Rm.

The Fourier transform of the turbulent motion $\boldsymbol{u}(\boldsymbol{x},t)$ is given by

$$\tilde{\boldsymbol{u}}(\boldsymbol{k},\omega) = \frac{1}{(2\pi)^4} \int \int \boldsymbol{u}(\boldsymbol{x},t) e^{-i(\boldsymbol{k}\cdot\boldsymbol{x}-\omega t)} d\boldsymbol{x}\,dt. \tag{7}$$

By assuming that the statistics of $\boldsymbol{u}(\boldsymbol{x},t)$ are stationary and homogeneous, we can express its correlation function in terms of the spectrum tensor $\Phi_{ij}(\boldsymbol{k},\omega)$ as

$$\langle \tilde{u}_i(\boldsymbol{k},\omega)\tilde{u}_j^\star(\boldsymbol{k},\omega)\rangle = \Phi_{ij}(\boldsymbol{k},\omega)\delta(\boldsymbol{k}-\boldsymbol{k}')\delta(\omega-\omega'), \tag{8}$$

where $\langle \cdot \rangle$ is an ensemble average and the superscript $\star$ denotes the complex conjugate. For an isotropic helical flow, the spectrum tensor consists of a combination of the energy and helicity spectrum functions, $E(k,\omega)$ and $F(k,\omega)$, respectively, in the following form:

$$\Phi_{ij}(\boldsymbol{k},\omega) = \frac{E(k,\omega)}{4\pi k^2}(k^2\delta_{ij} - k_i k_j) + i\frac{F(k,\omega)}{8\pi k^2}\epsilon_{ijk}k_k. \tag{9}$$

In order to compute the mean emf, we use FOSA to simplify Eq. (6) by neglecting the interactions between small-scale quantities. In Fourier space, it becomes

$$(-i\omega + \eta k^2 + i(\boldsymbol{U}_0\cdot\boldsymbol{k}))\tilde{\boldsymbol{b}} = i(\boldsymbol{B}_0\cdot\boldsymbol{k})\tilde{\boldsymbol{u}}, \tag{10}$$

leading to the mean emf

$$\mathcal{E}_i = \int\int\int\int \frac{-i(\boldsymbol{B}_0\cdot\boldsymbol{k}')\epsilon_{ijk}\langle\tilde{u}_j(\boldsymbol{k},\omega)\tilde{u}_k^\star(\boldsymbol{k}',\omega')\rangle}{\eta k'^2 + i(\boldsymbol{U}_0\cdot\boldsymbol{k}'-\omega')}$$
$$\times e^{(i(\boldsymbol{k}-\boldsymbol{k}')\cdot\boldsymbol{x}-i(\omega-\omega')t)}d\boldsymbol{k}d\boldsymbol{k}'d\omega d\omega'. \tag{11}$$

Using Eqs. (9) and (8), we can simplify Eq. (11) to find that

$$\alpha_{ij} = -\frac{1}{4\pi}\int\int \frac{k_i k_j}{k^2}\frac{F(k,\omega)}{\eta k^2 + i(\boldsymbol{U}_0\cdot\boldsymbol{k}-\omega)}dk d\omega. \tag{12}$$

For simplicity, we now assume that the turbulent velocity field has a single length scale $1/k_0$, i.e., $F(\boldsymbol{k},\omega)=\delta(k-k_0)F(\omega)$, with a Lorentzian frequency spectrum of the form

$$F(\omega) = \frac{\gamma}{(\omega-\omega_0)^2 + \gamma^2}. \tag{13}$$

Here γ is the decorrelation rate, which measures the dispersion of the frequencies around the characteristic frequency ω_0 in $F(\omega)$ and thus characterizes the stochasticity of the turbulence.

For $\boldsymbol{U}_0 = U_0\hat{\boldsymbol{y}}$ and $\boldsymbol{B}_0 = B_0\hat{\boldsymbol{y}}$, α_{22}, which is the only nontrivial component of the $\boldsymbol{\alpha}$ tensor, can be shown to become

$$\alpha_{22} = -\frac{k_{0y}^2}{4k_0^2}\frac{\eta k_0^2 + \gamma}{(\eta k_0^2 + \gamma)^2 + (U_0 k_{0y}-\omega_0)^2}, \tag{14}$$

where we have used complex integration and the fact that α_{22} is a real quantity. It is clear from Eq. (14) that for given ω_0, γ, $\boldsymbol{k}_0$ and η, α_{22} takes its maximum value when U_0 satisfies $U_0 k_{0y}-\omega_0=0$, i.e., when the Doppler shifted frequency vanishes. Furthermore, as $U_0 \to \infty$, α_{22} is significantly reduced, scaling as U_0^{-2}. This dependence on U_0 is reminiscent of the quenching of transport $\propto \omega^{-2}$ in wavelike turbulence with frequency ω [17]. This may not be so surprising since, as explained in Sec. I C, a uniform flow introduces new frequencies in the turbulence via Doppler shift and, for large U_0, these frequencies dominate.

Equation (14) also shows that the α effect depends on the characteristics of the turbulence: frequency ω_0, stochasticity γ, wavenumber $\boldsymbol{k}_0$ and on the magnetic diffusivity η. In particular, we note that irreversibility, through either finite Ohmic dissipation ($\eta \neq 0$) or stochasticity ($\gamma \neq 0$), is required for α_{22} to be nonzero when $U_0 k_{0y}-\omega_0 \neq 0$. That is, when η and γ tend to zero, $\alpha \to 0$ except if there is a resonance point in the domain of interest, which gives a nonzero α effect with the value

$$\alpha_{22} = -\frac{k_{0y}^2}{4k_0^2}\delta(U_0 k_y - \omega_0). \tag{15}$$

We would therefore expect resonances to be more pronounced for high conductivity and long correlation times. However, the validity of the first order smoothing approximation used to derive Eqs. (14) and (15) becomes questionable in this limit.

Finally, we note that similar results, including Eq. (14), still hold approximately when $\boldsymbol{U}_0$ is not uniform provided it varies on scales large compared to the turbulence.

III. MODEL AND METHOD

In this section, we describe the flow (1) used in our numerical simulations. We first detail the small-scale, chaotic flows $\boldsymbol{u}_k$, then we introduce successively the shear and the uniform flows used to model the large-scale motion $\boldsymbol{U}_{LS}$. Finally, we explain how we determine the α effect.

A. Family of chaotic flows

The chaotic flows we use are based on a motion of the form

$$\boldsymbol{u}(x,y,t) = (\partial_y\psi, -\partial_x\psi, -\psi), \tag{16}$$

with

$$\psi(x,y,t) = \sqrt{\frac{3}{2}}(\cos\{x+\epsilon\cos[\omega t + \phi(t)]\}$$
$$+ \sin\{y+\epsilon\sin[\omega t + \phi(t)]\}). \tag{17}$$

For $\phi(t)=0$, the motion is time-periodic and corresponds to the Galloway-Proctor CP-flow [34]. In this case, although Eq. (17) seems to involve a single frequency ω, the spectrum of the CP-flow contains not only ω but also its harmonics

$n\omega$, for all integers n. The amplitude of the nth harmonic roughly decreases $\propto |J_n(\epsilon)|^2$ as n increases, where J_n is the nth order Bessel function [35]. Since $|J_n|^2$ decreases rapidly with increasing n, the contributions from the first few harmonics only are expected to be important.

The time-dependent phase $\phi(t)$ is a piecewise constant function, which varies over an adjustable timescale τ; for $\tau = \infty$, $\phi(t)$ does not change, reducing Eq. (17) to the CP-flow (see [36] for a more detailed description of the model). We use the value of τ, which can be related to γ^{-1} in Eq. (14), as a measure of the degree of time decoherence in the flow. This model was introduced by [31] in order to study systematically the influence of time decorrelations on the α effect. Related studies have used "renovating flows," which are random velocity fields, renewed after a characteristic time τ and more amenable to statistical analysis (see, e.g., [37–39] and references therein). Alternatively, stochasticity can be introduces in the motion (16) by randomizing the amplitude of its components, as reported in a recent study by [40]; this approach is however not pursued here.

Spatially, the CP-flow consists in a 2π-periodic array of helical cells with a single well defined length scale, corresponding to the size of the computational domain. For such time-dependent, space-periodic velocity fields, it is natural to define the averaging operation as

$$\langle \boldsymbol{u} \rangle = \frac{1}{4\pi^2 T} \int_0^T \int_0^{2\pi} \int_0^{2\pi} \boldsymbol{u}(x,y,t) dx dy dt, \qquad (18)$$

for a sufficiently large time T.

In the present problem, we are interested in the effects of a large-scale motion on the transport properties of a small-scale chaotic flow. We thus generalize the motion (16) by reducing its length scale to $2\pi/k$, where k is an integer larger than 2. To this end, we define the flow $\boldsymbol{u}_k$ by

$$\boldsymbol{u}_k(x,y,t) = (\partial_y \psi_k, -\partial_x \psi_k, -r_k \psi_k), \qquad (19)$$

with

$$\psi_k(x,y,t) = A_k(\cos\{kx + \epsilon_k \cos[\omega_k t + \phi_k(t)]\}$$
$$+ \sin\{ky + \epsilon_k \sin[\omega_k t + \phi_k(t)]\}), \qquad (20)$$

where the phases $\phi_k(t)$ change over a timescale equal to τ_k. The flow $\boldsymbol{u}_k$ corresponds to a $k \times k$ array of helical cells in a 2π-periodic domain, as shown on the top left-hand panel of Fig. 1, which resembles a snapshot of the streamlines of $\boldsymbol{u}_k$ for $k=4$. In order to ensure that the results obtained for $k > 1$ can be meaningfully compared to existing results for $k = 1$, we rescale the k-dependent quantities so that the kinetic energy and the α effect are independent of k. Following [41], which contains a detailed description of the rationale for the scalings, this can be achieved by taking

$$A_k = \sqrt{\frac{3}{2}}/k, \quad \epsilon_k = \epsilon, \quad \omega_k = k\omega, \quad \tau_k = \tau/k, \quad r_k = k. \quad (21)$$

The relevant magnetic Reynolds number is that based on the scale of $\boldsymbol{u}_k$; it is defined as $\mathrm{Rm}_k = \mathrm{Rm}/k$, where Rm is the magnetic Reynolds number based on the total system size.
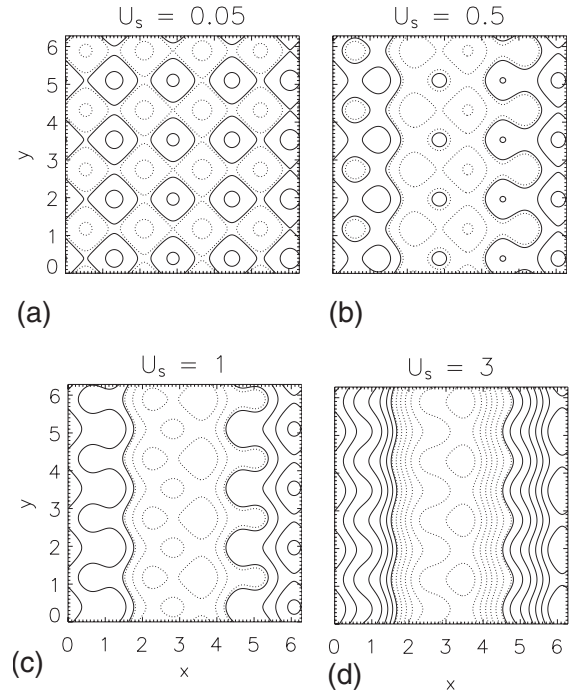

FIG. 1. Snapshot of the streamlines of $\boldsymbol{U}_{sh}(x,y,t)$ for increasing values of U_S: (a) 0.05, (b) 0.5, (c) 1, and (d) 3. The solid (dotted) lines correspond to positive (negative) values.

The numerical results in Sec. V are given exclusively in terms of Rm_k.

Finally, we note that for any k and τ_k, Eq. (18) gives

$$\langle \boldsymbol{u}_k \rangle = \boldsymbol{0}, \quad \langle \boldsymbol{u}_k \cdot \nabla \times \boldsymbol{u}_k \rangle = -3k,$$

$$\langle \|\boldsymbol{u}_k\|^2 \rangle = 3, \quad \langle \|\nabla \times \boldsymbol{u}_k\|^2 \rangle = 3k^2. \qquad (22)$$

Therefore, the relative kinetic helicity defined by

$$\mathcal{H}(\boldsymbol{u}) = |\langle \boldsymbol{u} \cdot \nabla \times \boldsymbol{u} \rangle| / (\langle \|\boldsymbol{u}\|^2 \rangle \langle \|\nabla \times \boldsymbol{u}\|^2 \rangle)^{1/2}, \qquad (23)$$

for a flow $\boldsymbol{u}$, is maximum (equal to 1) for the flows $\boldsymbol{u}_k$.

We restrict our numerical simulations to the case $\epsilon = \omega = 1$ and vary the parameters k, τ, and Rm_k. Within this model, we are able to generate chaotic flows on a scale $\propto k^{-1}$ and whose time correlations can be arbitrarily varied by changing the value of τ.

B. Large scale flows

1. Shear model

We model the large-scale shear flow by choosing $\boldsymbol{U}_{LS} = U_S \sin x \hat{\boldsymbol{y}}$, so that Eq. (1) becomes

$$\boldsymbol{U}(x,y,t) = \boldsymbol{U}_{sh}(x,y,t) = \boldsymbol{u}_k(x,y,t) + U_S \sin x \hat{\boldsymbol{y}}. \qquad (24)$$

The averaging rule (18) implies that for $k > 1$ we have

$$\langle \boldsymbol{U}_{sh} \rangle = \boldsymbol{0}, \quad \langle \boldsymbol{U}_{sh} \cdot \nabla \times \boldsymbol{U}_{sh} \rangle = -3k,$$

$$\langle \|\boldsymbol{U}_{sh}\|^2 \rangle = 3 + \frac{U_S^2}{2}, \quad \langle \|\nabla \times \boldsymbol{U}_{sh}\|^2 \rangle = 3k^2 + \frac{U_S^2}{2}. \quad (25)$$

The relative kinetic helicity $\mathcal{H}(\boldsymbol{U}_{sh})$ is thus a decreasing function of U_S.

Figure 1 presents snapshots of the streamlines of $\boldsymbol{U}_{sh}$ in the xy plane for increasing values of U_S. The cellular pattern characteristic of the CP-flow is clearly visible for weak shear. As U_S increases, the cells gradually give way to channels aligned with the direction of the shear flow.

In this model, resonances can occur when $n\omega_k - U_S k \sim 0$ for any integer n; Eq. (21) implies that this condition is independent of k and becomes

$$U_S \sim n \quad \text{with} \quad n = 1, 2, 3 \dots . \quad (26)$$

This estimate is based on the maximum value of the shear amplitude. Since the latter depends on x, however, for a given frequency ω, the resonance condition will be satisfied in finite regions of space for a range of values of U_S, thus leading to a broad resonance around $U_S \sim n$.

2. Uniform flow model

For the uniform flow model, we simply take $\boldsymbol{U}_{LS}$ to be a constant, uniform flow $\boldsymbol{U}_0$, of magnitude $U_0 = U_S / \sqrt{2}$, directed along the y axis. The velocity field (1) therefore becomes

$$\boldsymbol{U}(x, y, t) = \boldsymbol{U}_{un}(x, y, t) = \boldsymbol{u}_k(x, y, t) + U_S / \sqrt{2} \hat{\boldsymbol{y}}. \quad (27)$$

This choice ensures that for both models the large-scale motion is in the y direction and that $\langle \|\boldsymbol{U}_{un}\|^2 \rangle = \langle \|\boldsymbol{U}_{sh}\|^2 \rangle$. Using Eq. (18), we find that for $k > 1$

$$\langle \boldsymbol{U}_{un} \rangle = \boldsymbol{U}_0, \quad \langle \boldsymbol{U}_{un} \cdot \nabla \times \boldsymbol{U}_{un} \rangle = -3k,$$

$$\langle \|\boldsymbol{U}_{un}\|^2 \rangle = 3 + \frac{U_S^2}{2}, \quad \langle \|\nabla \times \boldsymbol{U}_{un}\|^2 \rangle = 3k^2. \quad (28)$$

The relative kinetic helicity $\mathcal{H}(\boldsymbol{U}_{un})$ is thus a decreasing function of U_S but remains independent of k. Owing to the rescaling (21), the α effect here is also independent of k and therefore, we mainly use $k = 1$ in our numerical simulations.

Figure 2 shows snapshots of the streamlines for flow (27) and increasing values of U_S. The cells characteristic of the CP-flow are progressively replaced by streamlines aligned with $\boldsymbol{U}_0$ as the latter increases in magnitude.

In this model, we expect to see resonances when $n\omega_k - U_0 k = n\omega_k - U_S k / \sqrt{2} \sim 0$ for any integer n. Using Eq. (21), this condition becomes

$$U_S \sim n\sqrt{2} \quad \text{with} \quad n = 1, 2, 3 \dots \quad (29)$$

and is independent of k.

C. Determination of the α effect

To determine the α effect for the shear model, we solve Eq. (6) with $\boldsymbol{u} = \boldsymbol{U}_{sh}$, given by Eq. (24), and $\boldsymbol{U}_0 = \boldsymbol{0}$. Clearly, in this model, the value of α depends on the scale separation between $\boldsymbol{U}_{sh}$ and $\boldsymbol{u}_k$, i.e., on k. To determine the α effect for
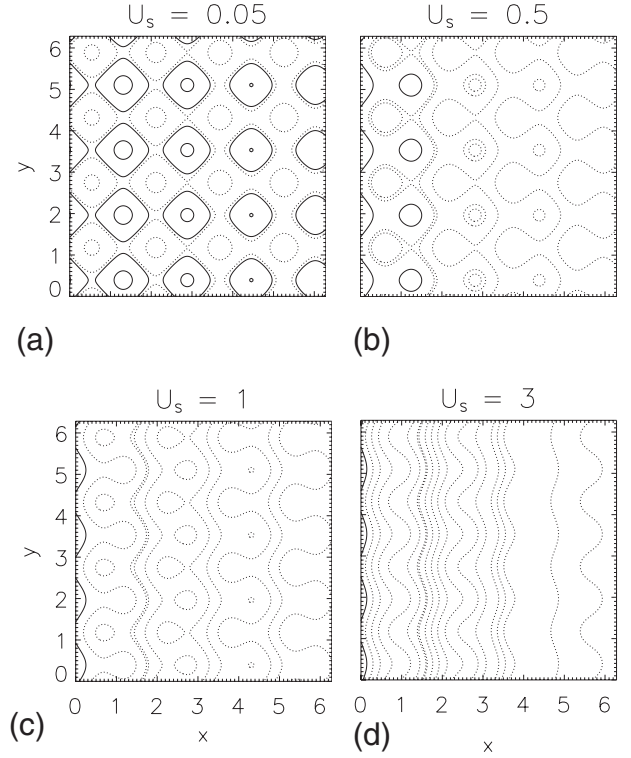

FIG. 2. Snapshot of the streamlines of $\boldsymbol{U}_{un}(x, y, t)$ for increasing values of U_0: (a) 0.05, (b) 0.5, (c) 1, and (d) 3. The solid (dotted) lines correspond to positive (negative) values.

the uniform flow model, we simply solve Eq. (6) with $\boldsymbol{u} = \boldsymbol{u}_k$ and $\boldsymbol{U}_0 \neq \boldsymbol{0}$.

In all cases, the initial condition is $\boldsymbol{b}(\boldsymbol{x}, 0) = \boldsymbol{0}$. Since the motions considered are independent of z, the small-scale field $\boldsymbol{b}(x, y, t)$ solution to Eq. (6) is generated by the distortion of $\boldsymbol{B}_0$ only (Cowling's theorem precluding any dynamo action [42]). As a result, $\boldsymbol{b}$ and $\boldsymbol{\mathcal{E}}$ are linearly and homogeneously related to the mean field $\boldsymbol{B}_0$ and the α effect is unambiguously defined by Eq. (5). Another advantage of our model is that since the calculation of the α effect reduces to a 2D problem, it is efficiently solved numerically, even for high values of Rm and on large computational domains.

The velocity fields we consider are independent of z, as a results, the α effect they drive acts solely in the xy plane and we can restrict our study to the 2×2 part of $\boldsymbol{\alpha}$ relating horizontal quantities. The CP-flow defined by Eqs. (16) and (17) is maximally helical, and is thus a good candidate for a strong α effect. It is invariant under a 90° rotation around the z axis with appropriate shifts in space and time. In the absence of a large-scale flow, the $\boldsymbol{\alpha}$ tensor, as a mean quantity, is similarly invariant and can be written as $\alpha_{ij} = \alpha \delta_{ij} - \gamma \epsilon_{ijk}$ (for more details see, e.g., [36]). The value of α is simply calculated by solving Eq. (6) with $\boldsymbol{U}_0 = \boldsymbol{0}$ and $\boldsymbol{B}_0 = B_0 \hat{\boldsymbol{x}}$ or $B_0 \hat{\boldsymbol{y}}$; in the latter case, we have $\alpha = \mathcal{E}_y B_{0y}^{-1}$. The α effect in the CP-flow has been determined for different values of the parameters ϵ, ω and Rm [31,32]. As mentioned above, we focus here on the case when $\epsilon = \omega = 1$. This choice ensures that the CP-flow is strongly chaotic [43] and possesses a strong kinematic α effect for most values of Rm. The same considerations apply to the flows $\boldsymbol{u}_k$ as α is independent of k.
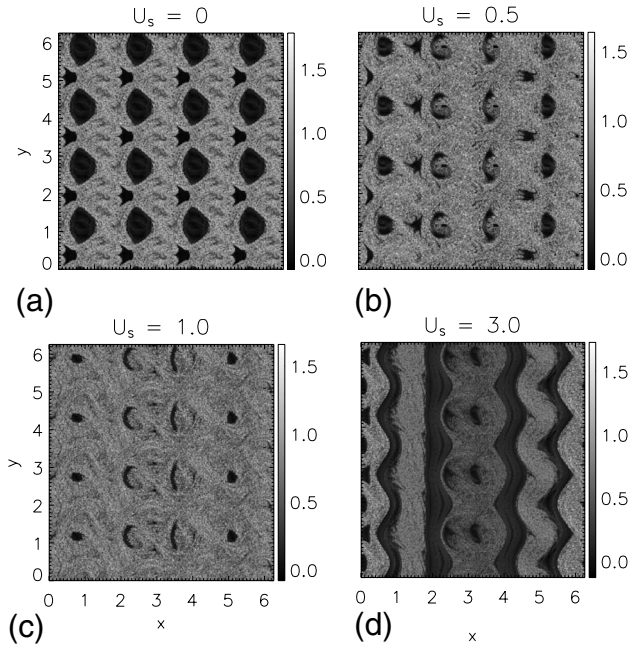
FIG. 3. Density plots of the finite-time Lyapunov exponents (t=25 time units) for the flow $\boldsymbol{U}_{sh}$ with k=4, τ=∞ and increasing values of U_S: (a) 0, (b) 0.5, (c) 1, (d) 3..

FIG. 4. Density plots of the finite-time Lyapunov exponents (t=25 time units) for the flow $\boldsymbol{U}_{sh}$ with k=4, τ=2π and increasing values of U_S: (a) 0, (b) 0.5, (c) 1, (d) 3.

As soon as we introduce the large-scale motion $\boldsymbol{U}_{LS}$, the symmetry between the x and y directions is lost, with $\alpha_{11} \neq \alpha_{22}$ in general. For our study, we exclude the possibility of any direct interaction between the large-scale velocity and magnetic fields. This is trivially ensured in the uniform flow model since both large-scale fields are constant vectors. For the shear model however, we need to choose the configuration of $\boldsymbol{B}_0$ such that $(\boldsymbol{B}_0 \cdot \nabla)(U_S \sin x \hat{\boldsymbol{y}}) = \boldsymbol{0}$. We thus take $\boldsymbol{B}_0 = B_0 \hat{\boldsymbol{y}}$ so that the mean field is parallel to the shear, and determine $\alpha_{22} = \mathcal{E}_y B_{0y}^{-1}$. All our simulations are restricted to the case when $\boldsymbol{B}_0$ is aligned with $\boldsymbol{U}_{LS}$. In the remainder of this paper, we drop the subscript and refer to α_{22} as α.

IV. CHAOTIC PROPERTIES OF THE FLOWS

For $\epsilon = \mathcal{O}(1)$ and $\omega = \mathcal{O}(1)$, the CP-flow displays substantial regions of Lagrangian chaos. We describe here how these are modified by the addition of a large-scale motion and by time decorrelations. Figs. 3 and 4 present density plots of the finite-time Lyapunov exponents (taken after 25 time units) in the shear model, with k=4, for increasing values of U_S and for τ=∞ and 2π, respectively. For τ=∞ and U_S=0, the density plots show the pattern of laminar islands and chaotic regions characteristic of the CP-flow (see the top left-hand panel of Fig. 3). As U_S increases, the chaotic regions become wider as the transport barriers formed in $\boldsymbol{u}_k$ are destroyed by the shear, which connects different ergodic regions. When the shear is strong enough to dominate over the small-scale flow, chaotic regions become separated by laminar channels oriented along the y direction (see the plot for U_S=3 in Fig. 3). Similar observations can be made for τ=2π (Fig. 4); however, owing to the increase in stochasticity, the laminar islands and channels are less pronounced. In particular, there
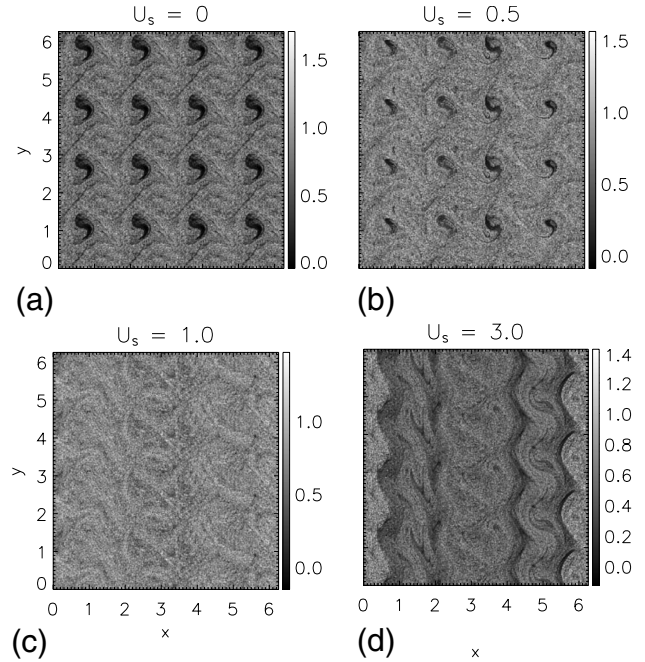
are no remaining islands for U_S=1 due to the combined effects of time decorrelations and shear. For both values of τ, we observe that the most uniform spatial distribution of Lyapunov exponents is found when the value of U_S is close to that corresponding to the main resonance point ($U_S \sim 1$). Qualitatively similar results are obtained for the uniform flow model.

Finally, Fig. 5 shows how the spatially averaged, finite-time Lyapunov exponent λ varies with increasing U_S, for both models, τ=∞ and 2π. For the shear model and both values of τ, λ varies little for $U_S < 1$ but is reduced for stron-
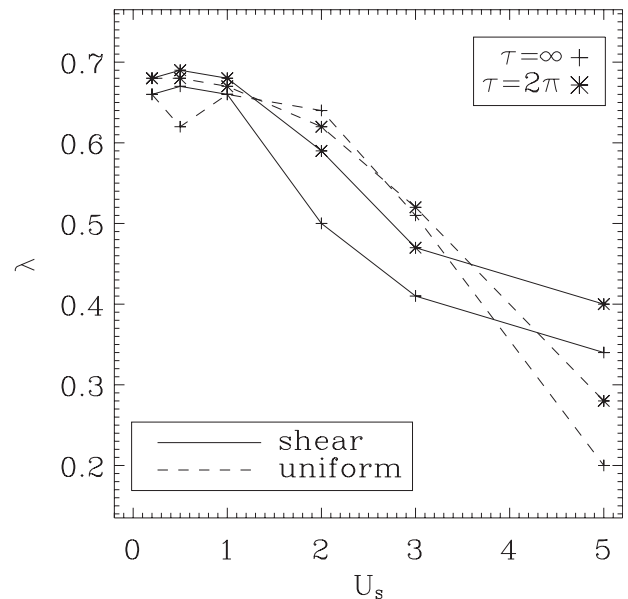

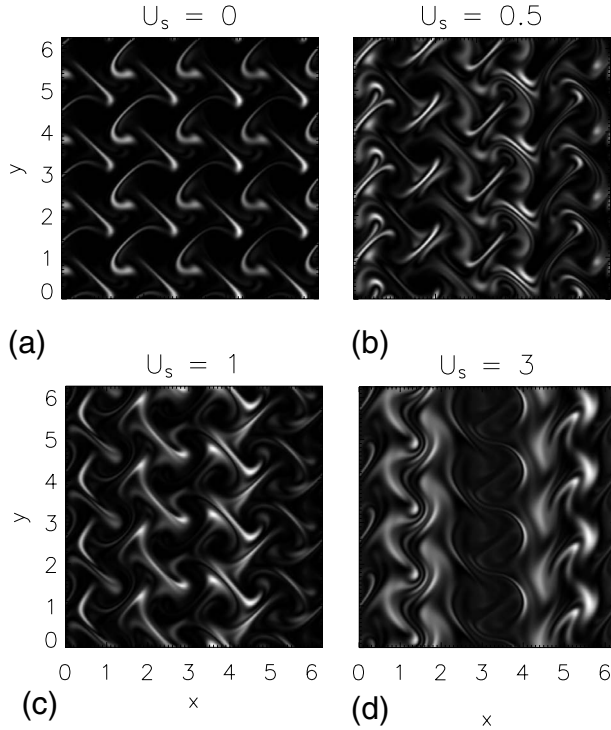FIG. 5. λ versus U_S for both models, τ=2π and ∞; k=4.

FIG. 6. Density plots of the magnetic energy normalized by its maximum value, for the shear model, $\tau=\infty$ and increasing values of U_S: (a) 0.05, (b) 0.5, (c) 1, (d) 3. The grayscale goes from 0 (black) to 1 (white); $k=4$, $\mathrm{Rm}_k=64$.
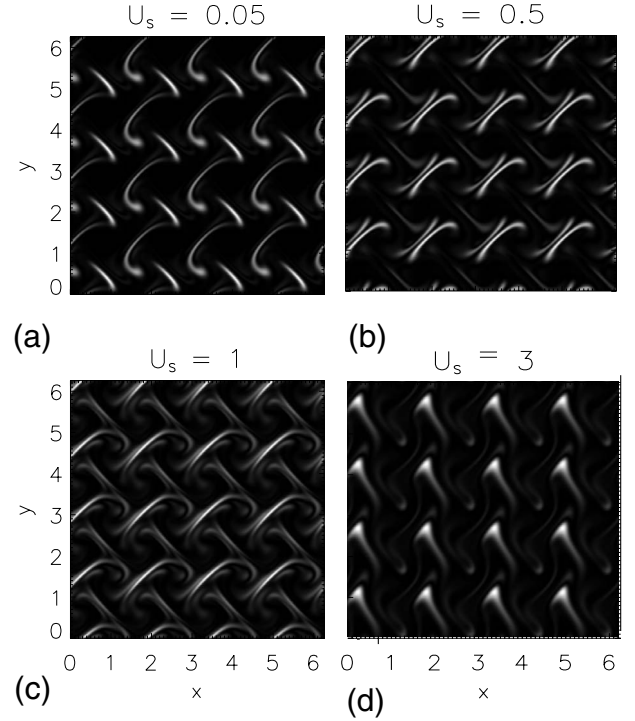

FIG. 7. Density plots of the magnetic energy normalized by its maximum value, for the uniform flow model, $\tau=\infty$ and increasing values of U_S: (a) 0.05, (b) 0.5, (c) 1, (d) 3. The grayscale goes from 0 (black) to 1 (white); $k=4$, $\mathrm{Rm}_k=64$.

ger shear. The value of λ for $\tau=2\pi$ is always higher than that for $\tau=\infty$, at least for the values of U_S investigated here. This is not surprising since the chaotic regions are more spatially extended for a more random flow (compare Figs. 3 and 4). For the uniform flow model, λ varies little for $U_S\leq 2$, except for a small decrease at $U_S=0.5$ for $\tau=\infty$. For larger values of U_S, λ decreases more steeply than for the shear model. In both models, it seems that for $U_S\leq 1$, the presence of a large-scale flow affects the spatial distribution of chaos rather than its average intensity.

V. NUMERICAL RESULTS

In this section we present the results of our numerical MHD simulations. We solve Eq. (6) using a 2D pseudospectral discretization in space and a second-order Runge-Kutta timestepping scheme. The code is optimized to run on machines with parallel architecture.

Most runs are done using $k=4$, $\mathrm{Rm}_k=64$ and varying U_S and τ. A few runs are also performed for the shear model at higher k ($k=16$, $\mathrm{Rm}_k=64$) and for both models at higher Rm ($k=4$, $\mathrm{Rm}_k=256$).

A. Magnetic field profile

We begin by illustrating how the small-scale magnetic field $\boldsymbol{b}(x,y,t)$ is influenced by a large-scale motion. Fig. 6 presents snapshots of the small-scale magnetic energy for the shear model, $U_S=[0.05,0.5,1,3]$ and $\tau=\infty$ (qualitatively similar results are obtained for shorter τ). For small shear,

concentrations of strong magnetic fields are spread throughout the computational domain, whereas for $U_S=3$, y-directed bands of lower magnetic activity appear. Comparison with Fig. 3 shows that the location of strong magnetic fields is related to the underlying Lagrangian structure of the flow. Furthermore, as U_S is increased, the magnetic structures tend to be elongated in the direction of the shear flow thus leading to an increase of the magnetic length scale in the y direction. The corresponding results for the uniform flow model are given in Fig. 7 where similar observations can be made. As expected here, the spatial period of the magnetic field is $2\pi/k$ in the x and y directions.

B. Small-scale magnetic energy

Figs. 8 and 9 show how $\langle b_H^2\rangle=\langle b_x^2+b_y^2\rangle$ varies with U_S, for different values of τ, in the shear and uniform flow models, respectively. The general trend is for $\langle b_H^2\rangle$ to decrease with increasing U_S, indicating that the presence of a large-scale flow inhibits the generation of strong magnetic fluctuations by shearing and sweeping.

For both models, when $U_S\leq 0.5$, $\langle b_H^2\rangle$ decreases only slightly with U_S while increasing with τ. Indeed, in a more random flow, field diffusion in the kinematic regime is likely to be enhanced by the bringing together of field lines of opposite polarity so that the magnitude of $\langle b_H^2\rangle$ is reduced. For $U_S>0.5$ however, this order is reversed: the curves for the shortest value of τ clearly lie above the others, the corresponding value of $\langle b_H^2\rangle$ decreasing monotonically as U_S increases. It seems therefore that the effects of the large-scale
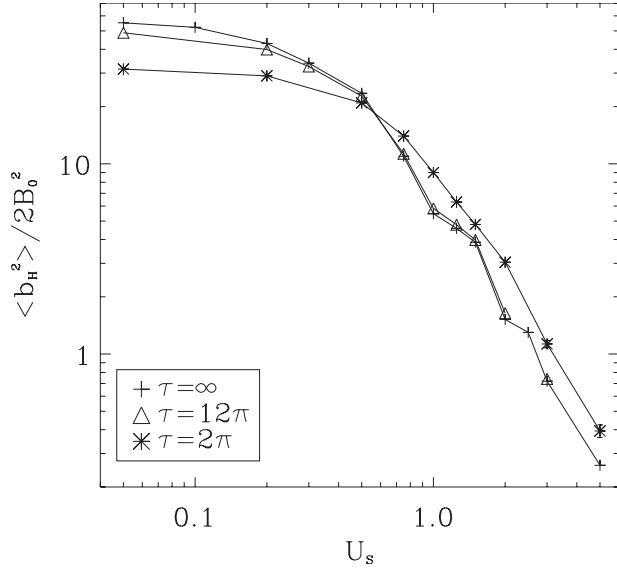
FIG. 8. $\langle b_H^2 \rangle / 2B_0^2$ versus U_S for the shear model and different values of τ, $k=4$, $\mathrm{Rm}_k=64$.

motion are more significant for less random flows. To examine this in more detail, we now focus on the behavior of $\langle b_H^2 \rangle$ for longer τ ($\tau=12\pi$ and ∞).

In the shear model, $\langle b_H^2 \rangle$ decreases with U_S at a rate ζ, which varies with U_S. Interestingly, it seems that ζ becomes smaller as U_S approaches (from $U_S=0$) the values satisfying the resonance condition (26) with $n=1$ or 2. The decrease in ζ is therefore probably due to a broad resonance. The same phenomenon appears more clearly in the uniform flow model where the resonance peaks are sharper. Specifically, the value of $\langle b_H^2 \rangle$ plateaus and even slightly increases when U_S satisfies the condition (29) with $n=1$ or 2. No resonances are clearly visible for higher values of n, owing to the small contribution of the corresponding frequencies to the spectrum of $\boldsymbol{u}_k$ (see Sec. III A).
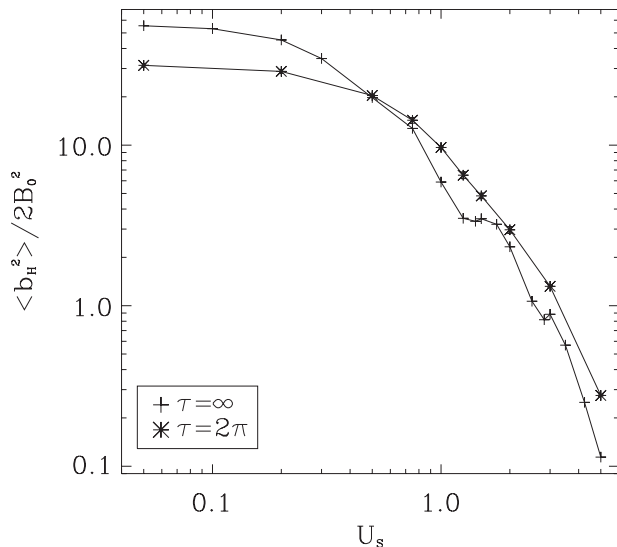
FIG. 9. $\langle b_H^2 \rangle / 2B_0^2$ versus U_S for the uniform flow model and different values of τ, $\mathrm{Rm}_k=64$. Compare with Fig. 8.
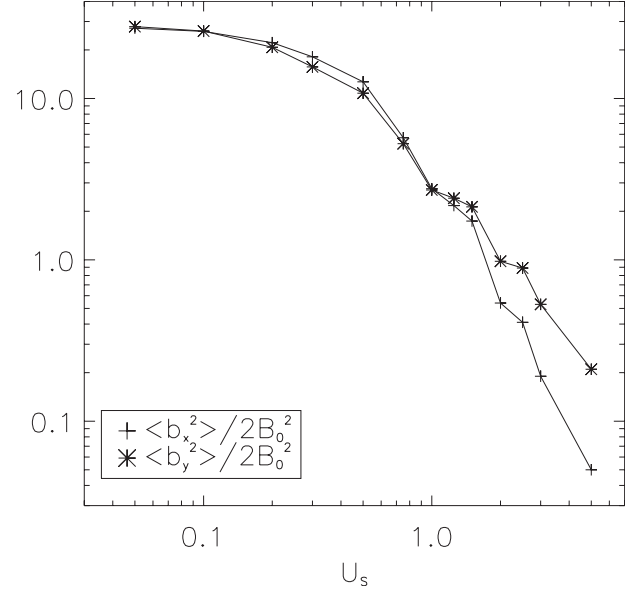
FIG. 10. $\langle b_x^2 \rangle / 2B_0^2 (+)$ and $\langle b_y^2 \rangle / 2B_0^2 (\star)$ versus U_S for the shear model; $\tau=\infty$, $k=4$, $\mathrm{Rm}_k=64$.

We now compare the magnitude of the x and y components of the small-scale magnetic field by showing how $\langle b_x^2 \rangle (+)$ and $\langle b_y^2 \rangle (\star)$ vary with U_S in the shear model (Fig. 10) and in the uniform flow model (Fig. 11), for $\tau=\infty$ (qualitatively similar results are obtained for shorter τ).

In the shear model, both components are of the same order of magnitude for $U_S \lesssim 1$, whereas for stronger shear $\langle b_y^2 \rangle$ dominates over $\langle b_x^2 \rangle$ and the difference between these two values is an increasing function of the shear amplitude. This result follows from the anisotropy introduced by the shear as it stretches b_x in the y-direction, thus creating a strong y component, while severely quenching the formation of the x component by shear distortion. This is consistent with previous works by [13,14] who predicted shear-induced weak, anisotropic turbulence.

In the uniform flow model, there is no such clear difference between $\langle b_x^2 \rangle$ and $\langle b_y^2 \rangle$. In this case, the large-scale motion only induces a drift but no direct stretching nor distortion of the magnetic structures. That is, anisotropy is one of the crucial difference between the effects of shear and mean flows [17].

Finally, we observe that here again the resonances are visible for both models.

C. α effect

1. Results for $\mathrm{Rm}_k=64$

In this section, we present the results for α rescaled by $U_{rms}=\langle U^2 \rangle^{1/2}$ for $k=4$ and $\mathrm{Rm}_k=64$, starting with the shear model. Figure 12 shows how α varies with U_S, for different values of $\tau (2\pi, 12\pi, 150, \infty)$. The dashed line corresponds to relative helicity $\mathcal{H}(U_{sh})$.

In all cases, α remains almost independent of the shear for U_S up to 0.2, then, as U_S increases, how α is affected by the shear depends on τ. For $\tau=2\pi$, α decreases monotonously with U_S, much faster than can be accounted for by a corre-
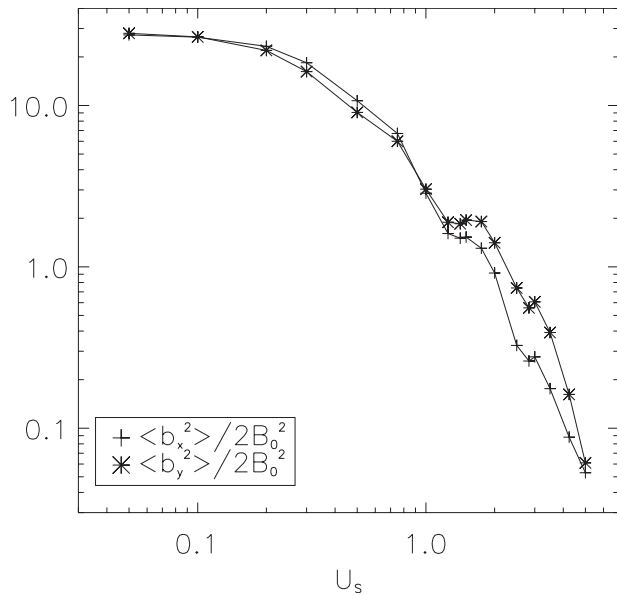
FIG. 11. $\langle b_x^2 \rangle / 2B_0^2 (+)$ and $\langle b_y^2 \rangle / 2B_0^2 (\star)$ versus U_S for the uniform flow model; $\tau = \infty$, $\mathrm{Rm}_k = 64$. Compare with Fig. 10.

sponding decrease in the relative helicity. For longer τ (12π, 150, ∞), α decreases sharply when $U_S = 0.5$ and increases again to reach a local maximum for $U_S = 1$, with a value for α still an order of magnitude lower than its value in the absence of shear. Finally, α decreases monotonously as U_S is increased further. The maximum observed for $U_S \sim 1$ is likely to be caused by a broad resonance, since it occurs when Eq. (26) is satisfied with $n = 1$. This is to be contrasted with the much sharper resonance peaks observed for the uniform flow model (see Fig. 14 below). This phenomenon is also visible for $\tau = 2\pi$, though much less pronounced. In this case, the chaotic flow's spectrum contains a wider range of frequencies, again leading to a less localized resonance.
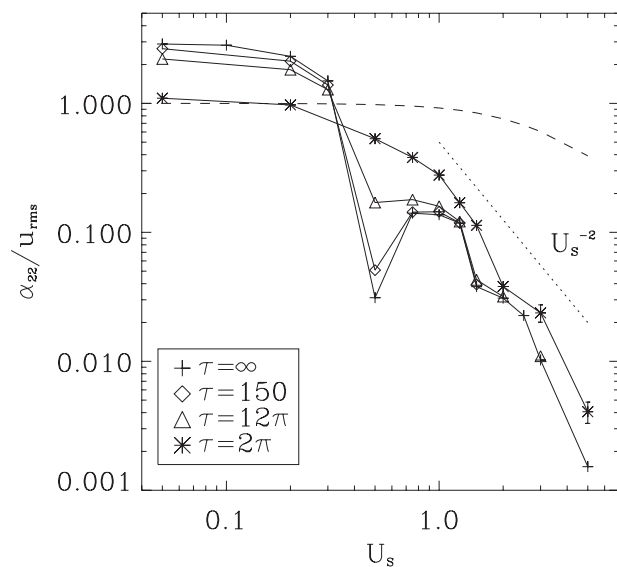

FIG. 12. α effect versus U_S in the shear model for different values of τ, $k = 4$, $\mathrm{Rm}_k = 64$. The dashed line gives the corresponding value of $\mathcal{H}(\boldsymbol{U}_{sh})$.
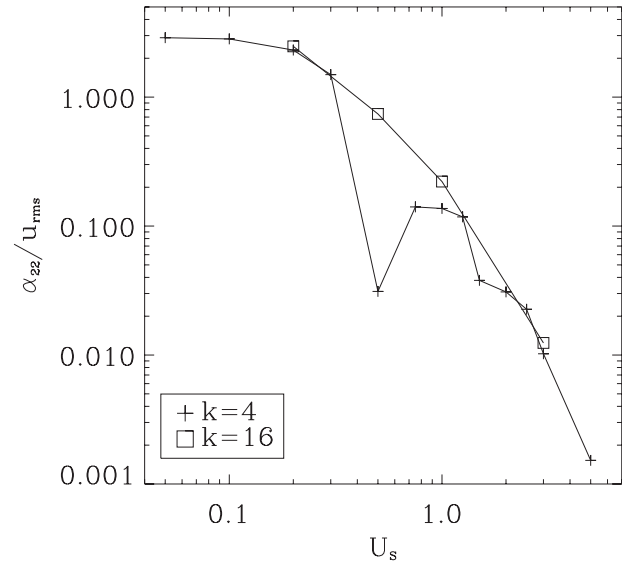

FIG. 13. α effect versus U_S in the shear model; $\tau = \infty$, $\mathrm{Rm}_k = 64$.

The sharp decrease in α for $U_S \sim 0.5$ in the case of long correlation times remains a puzzling feature. It appears to be caused by subtle interactions between modes at $k = 4$ and those at the scale of the computational domain. Indeed, in the absence of shear, all the energy of the $k = 4$ velocity modes will go toward the excitation of $k = 4$ magnetic modes. In the presence of a small shear however, some of the energy of the $k = 4$ velocity mode is diverted toward exciting magnetic modes with $k = 3$ or 5 through direct coupling with the $k = 1$ shear flow. Hence the α effect, which measures the correlations between $\boldsymbol{u}_k$ and $\boldsymbol{b}$, is diminished (recall that $\boldsymbol{u}_k$ contains only $k = 4$ mode). To investigate this matter further, we performed calculations for $\tau = \infty$, $\mathrm{Rm}_k = 64$, and $k = 16$. The results are presented in Fig. 13. Relations (21) imply that the only difference between our simulations for different values of k is the amount of scale separation between the large-scale shear and the chaotic flow. It appears that for $k = 16$ there is no sharp decrease in α around $U_S = 0.5$, with the results more similar to those obtained in the uniform flow model (see Fig. 14 below). One possible explanation for this is as follows. For a small-scale flow with $k = 4$, each of the $k = 4$ magnetic structures occupies a quarter of the entire domain, thus effectively experiencing the entire amplitude of the sinusoidal shear flow between $[0, U_S]$. Since shearing effects are independent of sign, all these structures are sheared in a similar way. For $k = 16$, however, each small-scale magnetic structure experiences only a quarter of the shear amplitude, with some of them being subjected to weak shear only. In this sense, increasing k leads us closer to the uniform flow $\boldsymbol{U}_{LS} \propto U_S \hat{\boldsymbol{y}}$ rather than the linear shear flow $\boldsymbol{U}_{LS} \propto U_S x \hat{\boldsymbol{y}}$.

We now turn to the description of the behavior of α in the uniform flow model. The results in this case are presented in Figs. 14 and 15, for $\tau = \infty$ and $\tau = 2\pi$ respectively. For $\tau = \infty$, α starts to decrease as soon as $U_S \gtrsim 0.3$, but this evolution is non monotonous, and localized resonances are visible for $U_S \sim 1.25$, 3 and even maybe $3\sqrt{2}$, the most pronounced peak being for $U_S \sim 3$. These values approximatively correspond
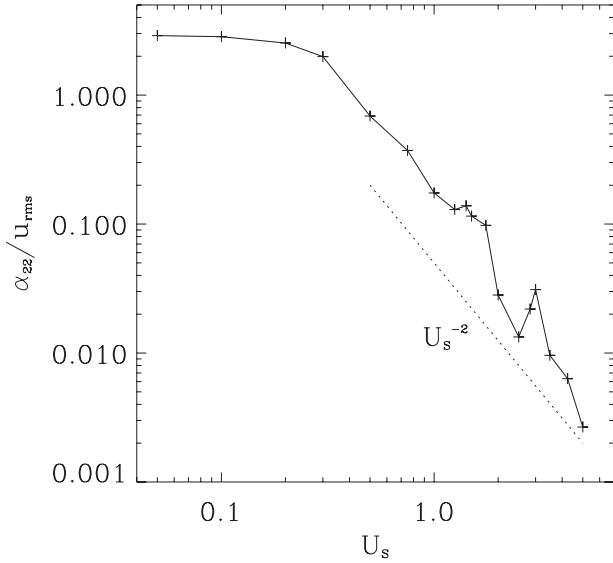
FIG. 14. α effect versus U_S in the uniform flow model; $\tau = \infty$, $Rm_k = 64$.

FIG. 16. α effect versus U_S in the shear model for different values of τ and Rm_k; $k = 4$.

to the condition (29) with $n = 1, 2$ or 3. For $\tau = 2\pi$, the results are qualitatively similar to those obtained in the shear model.

For both models and small U_S, α is an increasing function of τ. This behavior is reversed with larger values of α measured for shorter τ when $U_S \gtrsim 0.5$. To some extent, this phenomenon can be understood with reference to Eq. (14) (with U_S replacing U_0), even though it has been derived using FOSA, which is not strictly applicable to our simulations, especially for long τ.

When $U_S \to 0$ and in the short correlation time limit, i.e., $\gamma \gg \max(\omega_0, |\mathbf{U} \cdot \mathbf{k}|)$, Eq. (14) reduces to $\alpha \propto (\eta k^2 + \gamma)^{-1}$ so that α indeed decreases with the correlation time, which is proportional to γ^{-1}. For sufficiently strong shear however, i.e., in the limit $|\mathbf{U} \cdot \mathbf{k}| \gg \max(\omega_0, \gamma)$, $\alpha \propto (\eta k^2 + \gamma)/U_S^2$, so that α increases with γ, hence with decreasing correlation time.
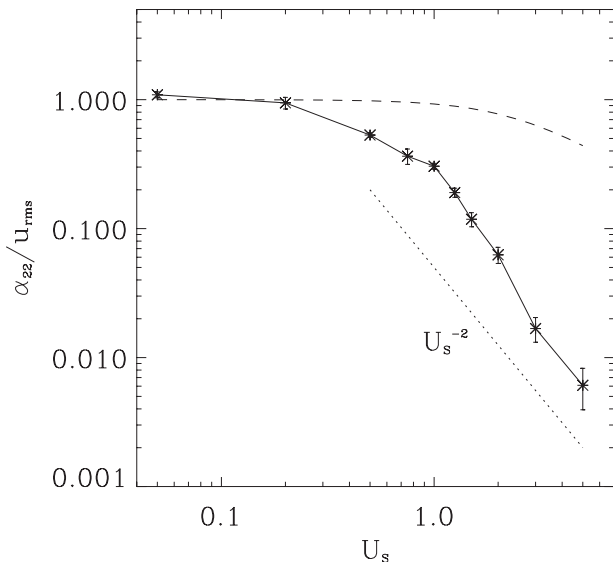

FIG. 15. α effect versus U_S in the uniform flow model; $\tau = 2\pi$, $Rm_k = 64$.

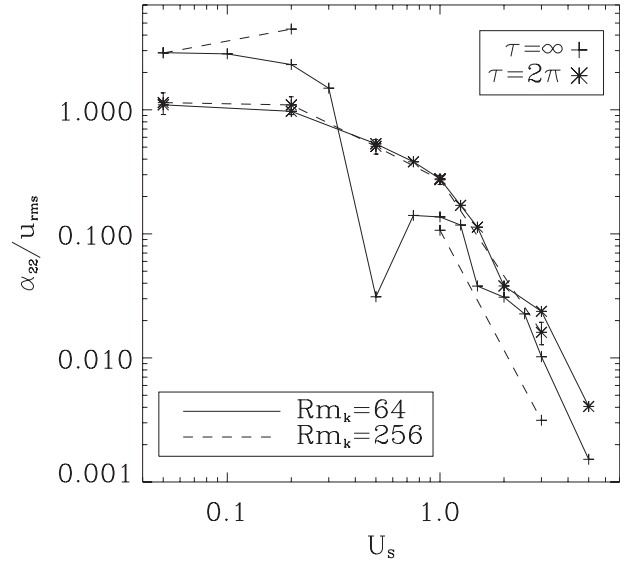This illustrates the fact that shear distortion is more efficient for coherent flows, leading to a more severe reduction in α. Note that the quenching of α as $U_S \to \infty$ scales as U_S^{-2}, as discussed at the end of Sec. II B. This scaling is shown by dotted lines on Figs. 12, 14, and 15. It appears that it is not far off from the way in which α decreases with U_S, although it is expected to be valid only in the limit of a strong amplitude of the large-scale motion.

2. Results for $Rm_k = 256$

To assess the robustness of the results described above, we also performed calculations at a higher magnetic Reynolds number, namely $Rm_k = 256$. The shear model results here are again obtained by using $k = 4$.

Figure 16 presents how α varies with U_S in the shear model, for $Rm_k = 256$ and two different values of τ (∞, and 2π, dashed lines); the corresponding results for $Rm_k = 64$ are shown for comparison (solid lines; these are the same results as in Fig. 12). For $\tau = 2\pi$, the results for both values of Rm superpose for most values of U_S (in agreement with [31] who showed that α becomes independent of Rm for short correlation time) and α decreases monotonically with U_S. For $\tau = \infty$ however, the results are remarkably different. For $Rm_k = 256$, α increases strongly as U_S is increased for small shear, then it changes sign, taking the value -0.68 for $U_S = 0.5$ (not shown). It then becomes positive again for $U_S = 1.0$ and subsequently decreases for stronger shear—at least for the values of U_S investigated here. These results are somewhat typical of the CP flow. That the α effect can change sign in this flow was first observed by [31], who also showed that this feature does not appear for short correlation times, as we observe here (see also [32]).

The corresponding results for the uniform flow model and $\tau = \infty$, presented in Fig. 17, are qualitatively different. The value of α first increases for small shear, then it is quenched, similarly to what happens for $Rm_k = 64$, without changing

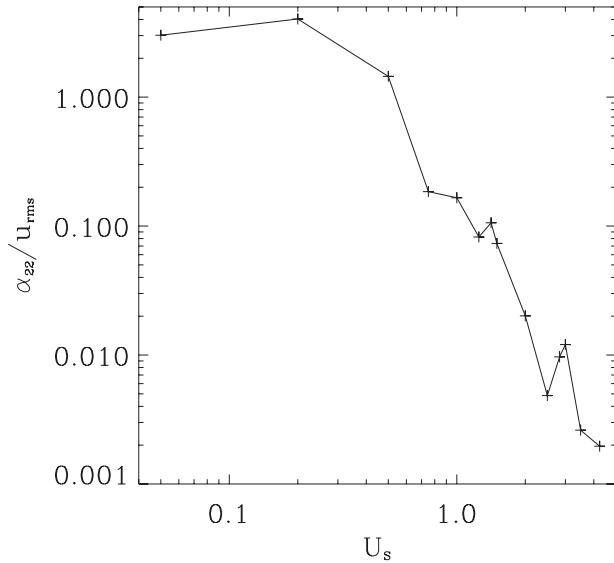FIG. 17. α effect versus U_S in the uniform flow model; $\tau = \infty$, $k=1$, $\mathrm{Rm}_k = 256$. Compare with Fig. 14.

sign. Resonances are again visible for $U_S \sim n\sqrt{2}$ with $n=1$ or 2, as expected from Eq. (29).

3. Temporal fluctuations in the mean emf

Many authors noted that the α effect is a very noisy quantity (e.g., [44–47]); in particular, [45] argued that its fluctuations should be taken into account in the mean-field equations. A recent model for large-scale dynamo action in the presence of shear, the "incoherent α-shear dynamo," does just this since it relies on the interactions between a large-scale shear flow and temporal variations in the α effect. This mechanism could account for large-scale dynamo action in situations when the α effect is small compared to its fluctuations [6,48–50]. It is therefore relevant to complete our study by analyzing the temporal variations of the spatially averaged emf; in particular, we determine how their amplitude depends on U_S.

To this end, we consider $E_y(t)$, the spatially averaged y component of the emf, rescaled by B_0 and U_{rms} [so the time average of $E_y(t)$ gives α/U_{rms}]. We only consider $\tau = 2\pi$ and $\mathrm{Rm}_k = 64$, since for $\tau = \infty$, the motion is periodic in time and large-scale dynamo action can be explained in terms of an α effect, regardless of the temporal oscillations in $E_y(t)$ [25]. Figs. 18 and 19 present the probability density functions (PDFs) of $E_y(t)$, for the shear and uniform flow models respectively and different values of U_S. In both cases, the PDFs become narrower as U_S increases, indicating a diminution in the amplitude of the temporal fluctuations. Figure 20 shows how the ratio, ξ say, of the time average of $E_y(t)$ (i.e., α) to its standard deviation varies with U_S. It appears that for the uniform flow model, ξ remains above 0.5 for $U_S \gtrsim 1$ and is sharply quenched for larger values of U_S. For the shear model, ξ increases for small U_S, reaching a maximum close to 1 for $U_S = 0.75$ and decreases thereafter (except possibly around $U_S = 3$).

For the models considered here, it seems that, for small U_S, the mean value of α remains substantial and is expected
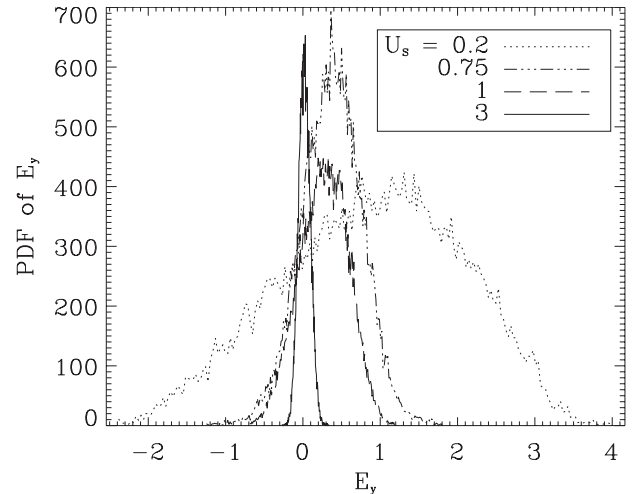

FIG. 18. PDF of $E_y(t)$ in the shear model; $\tau = 2\pi$, $\mathrm{Rm}_k = 64$.

to play a dominant role in the large-scale dynamo process. For larger values of U_S the situation is different and it is possible that incoherent α-shear processes play a more important part. This issue cannot however be addressed within the framework of this paper.

VI. DISCUSSION

In this paper, we presented a systematic numerical study of the influence of a large-scale motion $\boldsymbol{U}_{LS}$, either shear or uniform flow, on the kinematic α effect driven by small-scale chaotic flows. Our study, which is restricted to the situation when $\boldsymbol{U}_{LS}$ is parallel to the mean magnetic field, shows that the α effect is quenched by the presence of a strong, large-scale motion. We also found that α can be enhanced via resonances, which are more pronounced in the case when the large-scale flow is uniform and the small-scale velocity field has a long correlation time. The presence of the large-scale motion also reduces the magnitude of the magnetic fluctuations. We also considered how the large-scale flow affected
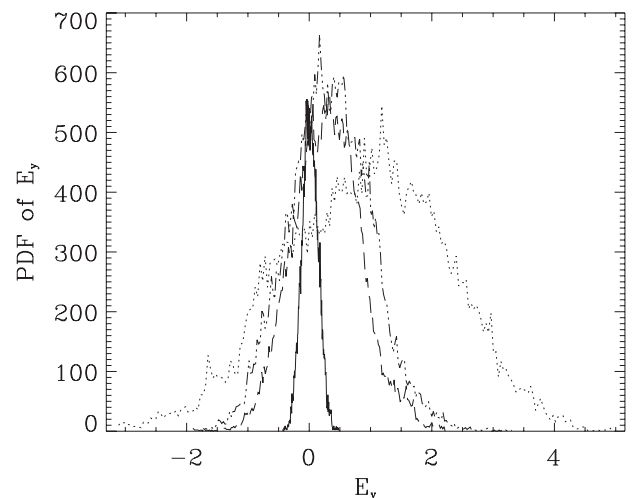

FIG. 19. PDF of $E_y(t)$ in the uniform flow model; $\tau = 2\pi$, $\mathrm{Rm}_k = 64$. The legend is given on Fig. 18.
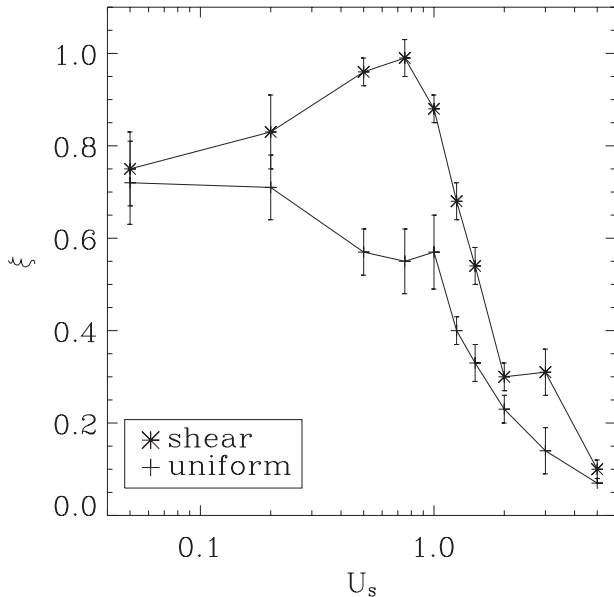
FIG. 20. ξ versus U_S for both models; $\tau = 2\pi$, $Rm_k = 64$.

the temporal fluctuations in α for simulations with $\tau = 2\pi$. Our results clearly demonstrate that large-scale flows can have a strong influence on the dynamics of the small-scales, thus affecting their transport properties, and should not be neglected.

We acknowledge that our study is limited to the specific family of chaotic motions we used and to a restricted parameter regime. In particular, it is notorious that the α effect in the Galloway-Proctor CP-flow depends strongly on the flow parameters and on Rm in situations far from the integrable limit [31,32]. The results we obtained for $Rm_k = 256$ and $\tau = \infty$ in the shear model are typical of this high variability. We note though that our aim was not to perform yet another detailed study of the CP-flow but rather to pinpoint shear-induced effect, providing solid numerical verification of previous theoretical predictions. In particular, we clearly demonstrated the α-quenching and the possibility of resonances due to the influence of a large-scale motion [18,22] and showed how these effects depended on the time statistics of the small-scale flows.

With the aim of modeling more realistic situations, the present work can be extended in the following several ways. First, it would be interesting to incorporate self-consistently the effects of the large-scale motion on the small-scale flow by obtaining the latter as a solution of the momentum equa-

tion, including the effects of large-scale advection. Then, in the spirit of [22] (see also [51]), the next step would be to add the effects of the Lorentz force in order to study the nonlinear regime and the influence of a dynamical mean field on large-scale dynamo action.

One could also consider more realistic small-scale velocity fields, such as 3D MHD turbulence. However, there are issues concerning the calculation and interpretation of the α effect in the case when the turbulence is capable of small-scale dynamo action, which is likely to be the case for 3D flows, even at moderate values of the magnetic Reynolds number [52].

Lastly, recall that in this paper the large-scale flow was taken to be aligned with the mean magnetic field and we only determined one component of the $\boldsymbol{\alpha}$ tensor. Combined with shear, this component (or its temporal fluctuations) can lead to large-scale dynamo action. However, in the absence of shear, it is necessary to calculate all the components of the symmetric part of $\boldsymbol{\alpha}$ to determine the efficiency of the large-scale dynamo process (via a so-called α^2-mechanism) and thus we need to consider the case when the mean magnetic field and the large-scale flow are perpendicular to each other, as was done by [28].

Finally, the large-scale shear in our study was taken to be a y-directed, x-dependent sine wave at the size of the computational domain, while most of our simulations were performed for a small-scale flow with $k = 4$. It is thus questionable whether there was enough scale separation between large-scale shear and small-scale flow. When we ran simulations with $k = 16$, the results were similar to those obtained with the uniform flow model. That is, the increased scale separation gave us a mixture of effects induced by shear and by large-scale advection. This effect is likely to persist in realistic turbulence containing a broad range of scales, where smaller eddies are both sheared and advected by larger ones.

[1] H. K. Moffatt, in *Magnetic Field Generation in Electrically Conducting Fluids* (Cambridge University Press, Cambridge, England, 1978).

[2] F. Krause and K.-H. Rädler, *Mean Field Magnetohydrodynamics and Dynamo Theory* (Pergamon Press, New York, 1980).

[3] *The Solar Tachocline*, edited by D. W. Hughes, R. Rosner, and N. O. Weiss (Cambridge University Press, Cambridge, En-

gland, 2007).

[4] I. Rogachevskii and N. Kleeorin, Phys. Rev. E **68**, 036301 (2003).

[5] I. Rogachevskii and N. Kleeorin, Phys. Rev. E **75**, 046305 (2007).

[6] A. Brandenburg, K.-H. Rädler, M. Rheinhardt, and P. J. Käpylä, Astrophys. J. **676**, 740 (2008).

[7] K. H. Burrell, Phys. Plasmas **4**, 1499 (1997).

[8] P. W. Terry, Rev. Mod. Phys. **72**, 109 (2000).

[9] E. Kim, Mod. Phys. Lett. B **18**, 551 (2004).

[10] E. Kim, T. S. Hahm, and P. H. Diamond, Phys. Plasmas **11**, 4554 (2004).

[11] C. Fenzi *et al.*, Phys. Plasmas **12**, 062307 (2005).

[12] Y. Andrew *et al.*, Plasma Phys. Controlled Fusion **48**, 479 (2006).

[13] E. Kim, Astron. Astrophys. **441**, 763 (2005).

[14] N. Leprovost and E. Kim, Astron. Astrophys. **456**, 617 (2006).

[15] E. Kim and N. Leprovost, Astron. Astrophys. **465**, 633 (2007).

[16] N. Leprovost and E. Kim, Astron. Astrophys. Lett. **463**, L9 (2007).

[17] N. Leprovost and E. Kim, Phys. Rev. E **78**, 016301 (2008).

[18] N. Leprovost and E. Kim, Phys. Rev. Lett. **100**, 144502 (2008).

[19] R. T. D. Mitra, P. J. Käpylä, and A. Brandenburg, Astron. Astrophys. **495**, 1 (2009).

[20] E. Kim and B. Dubrulle, Phys. Plasmas **8**, 813 (2001).

[21] E. Kim, Phys. Rev. Lett. **96**, 084504 (2006).

[22] A. P. L. Newton and E. Kim, Phys. Rev. Lett. **102**, 165002 (2009).

[23] M. G. Shats, H. Xia, H. Punzmann, and G. Falkovich, Phys. Rev. Lett. **99**, 164502 (2007).

[24] B. Dubrulle and U. Frisch, Phys. Rev. A **43**, 5355 (1991).

[25] G. O. Roberts, Philos. Trans. R. Soc. London, Ser. A **266**, 535 (1970).

[26] A. J. Majda and P. R. Kramer, Phys. Rep. **314**, 237 (1999).

[27] G. O. Roberts, Philos. Trans. R. Soc. London, Ser. A **271**, 411 (1972).

[28] S. Childress and A. M. Soward, J. Fluid Mech. **205**, 99 (1989).

[29] A. M. Soward and S. Childress, Philos. Trans. R. Soc. London, Ser. A **331**, 649 (1990).

[30] A. Tilgner, Phys. Rev. Lett. **100**, 128501 (2008).

[31] A. Courvoisier, D. W. Hughes, and S. M. Tobias, Phys. Rev. Lett. **96**, 034503 (2006).

[32] K.-H. Rädler and A. Brandenburg, Mon. Not. R. Astron. Soc. **393**, 113 (2009).

[33] J. M. Ottino, *The Kinematics of Mixing: Stretching, Chaos and Transport* (Cambridge University Press, Cambridge, England, 1989).

[34] D. J. Galloway and M. R. E. Proctor, Nature (London) **356**, 691 (1992).

[35] E. G. Zweibel and F. Heitsch, Astrophys. J. **684**, 373 (2008).

[36] A. Courvoisier, Geophys. Astrophys. Fluid Dyn. **102**, 217 (2008).

[37] P. Dittrich, S. A. Molchanov, D. Sokoloff, and A. Ruzmaikin, Astron. Nachr. **305**, 119 (1984).

[38] A. D. Gilbert and B. J. Bayly, J. Fluid Mech. **241**, 199 (1992).

[39] S. Childress and A. D. Gilbert, *Stretch, Twist, Fold: the Fast Dynamo* (Springer, New York, 1995).

[40] N. Kleeorin, I. Rogachevskii, D. Sokoloff, and D. Tomin, Phys. Rev. E **79**, 046302 (2009).

[41] F. Cattaneo and S. M. Tobias, Phys. Fluids **17**, 127105 (2005).

[42] T. G. Cowling, Mon. Not. R. Astron. Soc. **94**, 39 (1933).

[43] Y. Ponty, A. Pouquet, and P.-L. Sulem, Geophys. Astrophys. Fluid Dyn. **79**, 239 (1995).

[44] M. Ossendrijver, M. Stix, and A. Brandenburg, Astron. Astrophys. **376**, 713 (2001).

[45] A. Brandenburg and D. Sokoloff, Geophys. Astrophys. Fluid Dyn. **96**, 319 (2002).

[46] A. Brandenburg and K. Subramanian, Phys. Rep. **417**, 1 (2005).

[47] F. Cattaneo and D. W. Hughes, J. Fluid Mech. **553**, 401 (2006).

[48] N. A. Silant'ev, Astron. Astrophys. **364**, 339 (2000).

[49] M. R. E. Proctor, Mon. Not. R. Astron. Soc. **382**, L39 (2007).

[50] D. W. Hughes and M. R. E. Proctor, Phys. Rev. Lett. **102**, 044501 (2009).

[51] L. J. Silvers, Phys. Lett. A **334**, 400 (2005).

[52] F. Cattaneo and D. W. Hughes, Mon. Not. R. Astron. Soc. **395**, L48 (2009).